Accepted for Vehicle System Dynamics

Roll- and pitch-plane coupled hydro-pneumatic suspension. Part 2: Dynamic response analyses

Dongpu Cao[1]*, Subhash Rakheja[2] and Chun-Yi Su[2]

[1]*Waterloo Center for Automotive Research (WatCAR), Department of Mechanical and Mechatronics Engineering, University of Waterloo, Waterloo, Ontario, Canada*

[2]*CONCAVE Research Center, Department of Mechanical and Industrial Engineering Concordia University, Montreal, Quebec, Canada*

E_mails: dongpu@uwaterloo.ca; rakheja@alcor.concordia.ca; cysu@alcor.concordia.ca
*Corresponding author. Fax: 1-514-848-8635

Abstract: In the first part of this study, the potential performance benefits of fluidically-coupled passive suspensions were demonstrated through analyses of suspension properties, design flexibility and feasibility. In this second part of the study, the dynamic responses of a vehicle equipped with different configurations of fluidically-coupled hydro-pneumatic suspension systems are investigated for more comprehensive assessments of the coupled suspension concepts. A generalized 14 degree-of-freedom (DOF) nonlinear vehicle model is developed and validated to evaluate vehicle ride and handling dynamic responses, and suspension anti-roll and anti-pitch characteristics under various road excitations and steering/braking maneuvers. The dynamic responses of the vehicle model with the coupled suspension are compared with those of the unconnected suspensions to demonstrate the performance potentials of the fluidic couplings. The dynamic responses together with the suspension properties suggest that the full-vehicle coupled hydro-pneumatic suspension could offer considerable potential in realizing enhanced ride and handling performance, as well as improved anti-roll and anti-pitch properties in a very flexible and energy-saving manner.

Keywords: interconnected suspension; nonlinear vehicle model; ride; handling; anti-roll; anti-pitch

1. Introduction

The steering and/or braking maneuvers of road vehicles, particularly the heavy vehicles, generally induce comprehensive magnitudes of vehicle roll and/or pitch motions, and thus possibly the large lateral and/or longitudinal load transfers, e.g. in partially-filled

heavy tank vehicles [1-4]. While the rotational motions together with the road roughness-induced translational motions adversely influence the ride comfort, the dynamic load transfers affect the normal tire forces and thus the cornering and braking forces developed by the tires. These changes directly influence the directional and braking dynamic responses and stability limits of road vehicles generally in an undesirable manner [1-4]. Furthermore, the excessive pitch motions of the vehicle could adversely affect the driver's perception of the path and preview ability [5]. The importance of controlling the vehicle attitude (roll and pitch motions) has been emphasized in a number of studies, in order to improve the roll stability limit, path perception ability of the driver with minimal effort, and magnitudes of vehicle body motions in response to directional maneuvers and excitations arising from road and/or crosswinds [1, 2, 5, 6].

The anti-roll and anti-pitch characteristics of the vehicle suspension system, and thus inhibition of the dynamic lateral and longitudinal load transfers, form an important design objective. Moreover, the suspension design must provide adequate attenuation of the road-induced vibration and shock for preservation of health, safety and comfort of the driver/passengers, and protection of the cargos. The primary goal for road vehicle suspension design is thus to seek a satisfying compromise solution that can provide adequate control of ride vibration, and roll and pitch motions arising from different maneuvers and external excitations. Although numerous controlled suspension concepts have evolved over the past four decades to attain better compromise among the difference performance measures [7, 8], their implementations have been limited to cases where the additional cost, complexity and weight could be justifiable.

Alternate concepts in passive suspensions that can provide improved design

compromise are considered to be more desirable because of their simplicity and greater reliability. In the first part of this study, the performance potentials of concepts in hydro-pneumatic suspensions, with fluidic coupling either in the roll- or pitch-plane or in both the planes, have been discussed [9]. Considering the numerous possibilities of the fluidic couplings among four suspension strut units in the 3-dimensions, a feasibility analysis approach was proposed to obtain a preliminary assessment of different fluidically-coupled suspension configurations in view of their fundamental bounce, roll, pitch, and warp mode properties. The validity of the proposed methodology was also demonstrated through analyses of properties of a few selected coupled suspension configurations. The proposed methodology facilitated identification of feasible and potentially beneficial full-vehicle interconnected hydro-pneumatic suspension configurations. The results suggested that such passive fluidically-coupled hydro-pneumatic suspensions offer greater design flexibility and decoupling among the various fundamental stiffness/damping properties.

In this second part of the study, the dynamic response characteristics of selected fluidically-coupled full-vehicle hydro-pneumatic suspension configurations are investigated under steering/braking maneuvers and a wide range of road excitations. For this purpose, a nonlinear full-vehicle model incorporating the generalized fluidically coupled suspension is developed and validated using the measured data reported in published studies. The directional, roll and pitch dynamic responses are assessed under two critical handling maneuvers: braking-in-a-turn and split-μ straight-line braking. The ride and suspension travel responses are further evaluated under inputs arising from a range of road roughness and vehicle speeds.

2. Formulation of a Nonlinear Full-Vehicle Model

A range of linear and nonlinear models of road vehicles have been reported in the literature for analyses of ride, handling and directional control characteristics [e.g., 1-4]. The simple linear road vehicle models are known to provide reasonably good predictions of handling responses under lateral acceleration magnitudes up to 0.3g [10]. The studies reporting field-measured handling properties of heavy vehicle, however, have noted peak lateral acceleration magnitudes up to 0.8g [10, 11]. Another study has reported that a linear handling analysis of heavy vehicles may be considered valid only up to lateral accelerations of about 0.1g [2], since such high center of gravity (c.g.) vehicles could generate substantial load transfers across the axles under lateral acceleration above 0.1g. Although linear yaw plane models have been widely employed for handling analyses, considerations of longitudinal and lateral load transfers are considered essential for predicting handling and directional dynamic responses of heavy road vehicles [4, 12].

2.1 Development of a Nonlinear Full-Vehicle Model

In this study, a generalized 14-DOF model of a two-axle vehicle, incorporating uncoupled and selected configurations of the coupled hydro-pneumatic suspension, is developed to investigate dynamic responses to steering and braking inputs, as well as excitations arising from road roughness and/or crosswinds. The vehicle model, shown in Fig. 1, includes six DOFs of the sprung mass, two DOFs (bounce and roll) of each of the unsprung mass, and four rotational DOFs of the tire-wheel assemblies. The sprung mass is assumed to rotate about its roll axis [1, 13, 14].

The model incorporates the essential deflection modes of the sprung and unpsrung

rigid-bodies in a relatively simpler manner as opposed to elaborate multi-body dynamic models [e.g., 10]. The 14-DOF vehicle model is considered as a good compromise between high computational efficiency and accurate predictions of the dynamic response characteristics [15, 16]. Moreover, the proposed vehicle model offers the essential flexibility for modeling the nonlinear stiffness and damping properties of the fluidically-coupled hydro-pneumatic suspensions, and the vehicle responses to normal force inputs, such as those developed by of a semi-active/active suspension or controlled anti-roll bar systems. The model formulations also include the loss of tire-road contact and the response characteristics could thus be considered valid even after a wheel lift-off has occurred. The model may thus be applicable for assessments of rollover prevention strategies [17, 18]. The nonlinear braking and cornering forces developed by the tires are evaluated as functions of the normal load, slip angle and slip ratio using the Magic Formula tire model, which has been widely accepted as a leading tire model [4, 19, 20]. The nonlinear stiffness and damping forces and moments due to fluidically-coupled suspension struts are incorporated using the generalized model presented in [9, 21].

The vehicle attitude and position with respect to the inertial system *XYZ* are derived through successive coordinate-transformations through Euler angles (roll θ, pitch φ, and yaw ψ) [16, 22]. An identical front-wheel steering input (δ_f) is assumed for both the front wheels, while the rear-wheel steering input (δ_r) could also be conveniently included in the vehicle model, for analyses of vehicles with four-wheel-steering (4WS).

The full-vehicle model includes total forces developed by suspension struts, comprising the static as well as dynamic force components of the front-left (F_{fl}), front-rear (F_{fr}), rear-left (F_{rl}) and rear-right (F_{rr}) struts. The vertical properties of pneumatic tires are

represented by linear stiffness (k_{tf}, k_{tr}) and damping (c_{tf}, c_{tr}) elements, assuming point-contact with the road surface. Assuming small motions, the equations of motion for the sprung (m_s) and unsprung masses (m_{uf}, m_{ur}) are formulated using Lagrangian dynamics, and summarized as:

$$
\begin{aligned}
&m_s\left(\dot{u}+wq-vr+\dot{w}\varphi-vq\theta\right)=-\left(f_{yfl}+f_{yfr}\right)sin\,\delta_f-\left(f_{xfl}+f_{xfr}\right)cos\,\delta_f\\
&-\left(f_{yrl}+f_{yrr}\right)sin\,\delta_r-\left(f_{xrl}+f_{xrr}\right)cos\,\delta_r\\
&m_s\left(\dot{v}+ur-wp-\dot{w}\theta+uq\theta\right)=\left(f_{yfl}+f_{yfr}\right)cos\,\delta_f-\left(f_{xfl}+f_{xfr}\right)sin\,\delta_f\\
&+\left(f_{yrl}+f_{yrr}\right)cos\,\delta_r-\left(f_{xrl}+f_{xrr}\right)sin\,\delta_r+\left(F_{fl}+F_{fr}\right)\theta_{uf}+\left(F_{rl}+F_{rr}\right)\theta_{ur}+f_{wind}\\
&m_s\left(\dot{w}+vp-uq\right)=m_s g-\left(F_{fl}+F_{fr}+F_{rl}+F_{rr}\right)-m_s\left(-\dot{u}\varphi+ur\theta+\dot{v}\theta+vr\varphi\right)\\
&I_x\dot{p}-\left(I_{yy}-I_z\right)qr=F_{fl}l_{sf}-F_{fr}l_{sf}+F_{rl}l_{sr}-F_{rr}l_{sr}-k_{fbar}\left(\theta-\theta_{uf}\right)-k_{rbar}\left(\theta-\theta_{ur}\right)\\
&+I_{xz}\left(\dot{r}+pq\right)+\left(I_{yy}q^2\theta+I_z r^2\theta-I_{xz}pr\theta\right)+h_1\left[m_s g\theta+f_{wind}\right]\\
&+h_1\left[-\left(f_{yfl}+f_{yfr}\right)\cos\delta_f+\left(f_{xfl}+f_{xfr}\right)\sin\delta_f-\left(f_{yrl}+f_{yrr}\right)\cos\delta_r+\left(f_{xrl}+f_{xrr}\right)\sin\delta_r\right]\\
&I_{yy}\dot{q}-\left(I_z-I_x\right)pr=F_{fl}l_f+F_{fr}l_f-F_{rl}l_r-F_{rr}l_r+I_z\left(\dot{r}\theta+r^2\phi\right)\\
&+I_{xz}\left(r^2-p^2+rq\theta-\dot{p}\theta-rp\phi\right)-I_x pq\theta\\
&+h\left[-\left(f_{yfl}+f_{yfr}\right)\sin\delta_f-\left(f_{xfl}+f_{xfr}\right)\cos\delta_f-\left(f_{yrl}+f_{yrr}\right)\sin\delta_r-\left(f_{xrl}+f_{xrr}\right)\cos\delta_r\right]\\
&I_z\dot{r}-\left(I_x-I_{yy}\right)pq=\left(f_{yfl}+f_{yfr}\right)l_f\cos\delta_f-\left(f_{xfl}+f_{xfr}\right)l_f\sin\delta_f-\left(f_{yrl}+f_{yrr}\right)l_r\cos\delta_r\\
&+\left(f_{xrl}+f_{xrr}\right)l_r\sin\delta_r-\left(f_{yfl}-f_{yfr}\right)l_{tf}\sin\delta_f-\left(f_{xfl}-f_{xfr}\right)l_{tf}\cos\delta_f\\
&-\left(f_{yrl}-f_{yrr}\right)l_{tr}\sin\delta_r-\left(f_{xrl}-f_{xrr}\right)l_{tr}\cos\delta_r+M_{fl}+M_{fr}+M_{rl}+M_{rr}\\
&-I_x\left(pr\theta-\dot{p}\phi\right)-I_{yy}\dot{q}\theta-I_{yy}qr\phi-I_{xz}\left(rq-\dot{p}+\dot{r}\phi-r^2\theta\right)+M_{wind}\\
&m_{uf}\ddot{z}_{uf}=m_{uf}g+F_{fl}+F_{fr}+k_{tf}\left(z_{0fl}+z_{0fr}-2z_{uf}\right)+c_{tf}\left(\dot{z}_{0fl}+\dot{z}_{0fr}-2\dot{z}_{uf}\right)\\
&m_{ur}\ddot{z}_{ur}=m_{ur}g+F_{rl}+F_{rr}+k_{tr}\left(z_{0rl}+z_{0rr}-2z_{ur}\right)+c_{tr}\left(\dot{z}_{0rl}+\dot{z}_{0rr}-2\dot{z}_{ur}\right)\\
&I_{uf}\ddot{\theta}_{uf}=-F_{fl}l_{sf}+F_{fr}l_{sf}+k_{fbar}\left(\theta-\theta_{uf}\right)-k_{tf}l_{tf}\left(z_{0fl}-z_{0fr}+2l_{tf}\theta_{uf}\right)\\
&-c_{tf}l_{tf}\left(\dot{z}_{0fl}-\dot{z}_{0fr}+2l_{tf}\dot{\theta}_{uf}\right)\\
&I_{ur}\ddot{\theta}_{ur}=-F_{rl}l_{sr}+F_{rr}l_{sr}+k_{rbar}\left(\theta-\theta_{ur}\right)-k_{tr}l_{tr}\left(z_{0rl}-z_{0rr}+2l_{tr}\theta_{ur}\right)\\
&-c_{tf}l_{tf}\left(\dot{z}_{0fl}-\dot{z}_{0fr}+2l_{tf}\dot{\theta}_{uf}\right)
\end{aligned}
\tag{1}
$$

The rotational motion of each wheel assembly is derived from the forces and moments acting on the wheel assembly, as shown in Fig. 1(b):

$$I_{wi}\dot{\omega}_i = f_{xi}R_i - T_{bi} \quad (i = fl, fr, rl, rr) \tag{2}$$

TABLE 1

FIGURE 1

Table 1 together with Figs. 1(a) and 1(b) describes some of the notations used in the above formulations. In the developed model, the lateral and longitudinal motions/inertias of the unsprung masses were not included in order to further simplify the vehicle model. The effects of such modeling assumption on vehicle responses were discussed in Ref. [16], and demonstrated to be slight up to 11 degrees sprung mass roll response (Figs. 8 and 9, Ref. [16]), based on the vehicle model and steering input used. Considering heavy vehicles usually experience much smaller roll angles, such assumption would be considered to be reasonable for the analyses in this study. However, the yaw inertias of the unsprung masses in the vehicle model, mainly considering that such yaw inertias might be relatively larger for heavy vehicles with long wheelbases. The notations f_{xi}, f_{yi} and M_i are braking force, cornering force and aligning moment developed by tire i (i=*fl*, *fr*, *rl*, *rr*), respectively. g is acceleration due to gravity, and z_{0i} represents the road elevation at the tire-road interface of tire i. I_x and I_{yy} are the roll and pitch mass moments of inertia of the sprung mass, respectively, I_z is

the yaw mass moment of inertia of the vehicle, and I_{xz} is pitch-plane cross moment of inertia. I_{uf} and I_{ur} are the roll mass moments of inertia of the front and rear unsprung masses, respectively. l_{sf} and l_{sr} are half lateral-spacing of the front and rear suspensions, respectively. l_{tf} and l_{tr} are half track-widths of the front and rear ends, respectively. l_f and l_r are longitudinal distances between the sprung mass c.g. and the front and rear axles, respectively. h and h_1 are the c.g. heights of the sprung mass from the ground and the roll axis, respectively. k_{fbar} and k_{rbar} are stiffness constants of the front and rear anti-roll bars, respectively. T_{bi} is applied braking torque, R_i is effective radius of tire i, and I_{wi} is polar mass moment of inertia of wheel i. The excitations arising from crosswinds are incorporated in the formulations by an equivalent force (f_{wind}) directly applied to the vehicle c.g. together with a yaw moment (M_{wind}) [23]. The rates of the Euler angles (roll θ, pitch φ, and yaw ψ) are derived from [16, 22]:

$$\begin{bmatrix} \dot{\theta} \\ \dot{\varphi} \\ \dot{\psi} \end{bmatrix} = \begin{bmatrix} p + r\varphi \\ q - r\theta \\ r + q\theta \end{bmatrix} \tag{3}$$

The Magic Formula tire model is used to derive braking and cornering forces, and aligning moment developed by a tire, as a function of the longitudinal-slip ratio and/or slip angle, and the normal tire load [20, 24, 25]. By assuming small steering angles, the longitudinal slip ratio (ss_i) and slip angle (α_i) used in the tire model can be expressed as:

$$ss_{fl} = \left(1 - \frac{R_{fl}\omega_{fl}}{u + w\phi + l_{tf}\dot{\psi}}\right); \quad ss_{fr} = \left(1 - \frac{R_{fr}\omega_{fr}}{u + w\phi - l_{tf}\dot{\psi}}\right)$$

$$ss_{rl} = \left(1 - \frac{R_{rl}\omega_{rl}}{u + w\phi + l_{tr}\dot{\psi}}\right); \quad ss_{rr} = \left(1 - \frac{R_{rr}\omega_{rr}}{u + w\phi - l_{tr}\dot{\psi}}\right)$$

$$\alpha_{fl} = \delta_f - \frac{v - w\theta + l_f\dot{\psi}}{u + w\varphi + l_{tf}\dot{\psi}}; \quad \alpha_{fr} = \delta_f - \frac{v - w\theta + l_f\dot{\psi}}{u + w\varphi - l_{tf}\dot{\psi}}$$

$$\alpha_{rl} = \delta_r - \frac{v - w\theta - l_r\dot{\psi}}{u + w\varphi + l_{tr}\dot{\psi}}; \quad \alpha_{rr} = \delta_r - \frac{v - w\theta - l_r\dot{\psi}}{u + w\varphi - l_{tr}\dot{\psi}} \tag{4}$$

2.2 Coupled Suspension Configurations and Formulations of Strut Forces

A number of full-vehicle interconnected hydro-pneumatic suspension systems involving single- as well as twin-gas-chamber strut designs have been conceived in the first part of the study [9], among which three configurations were selected on the basis of their fundamental stiffness and damping properties in the bounce, roll, pitch and warp modes. These selected suspension configurations are further summarized in Fig. 2, which include: C1 – involving hydraulic fluid couplings between the four single-gas-chamber struts; C2 – with pneumatic couplings between the four twin-gas-chamber struts; C3 – involving hybrid (hydraulic and pneumatic) couplings between the two twin-gas chamber struts (front suspension) and two single-gas chamber struts (rear suspension); and U1 – unconnected suspension employing single-gas chamber struts with integrated damping valves. The parameters of struts in the U1 configuration could be selected to yield properties similar to that of a conventional air spring and hydraulic damper suspension system. Since heavy vehicles invariably employ anti-roll bars, the U1 configuration with front and rear anti-roll bars is also considered for analyses, referred to as U1bar [9]. The strut forces, and stiffness and damping properties of the selected

suspension configurations have been derived using a generalized model [21], and presented in [9].

FIGURE 2

2.3 Method of Analysis

It has been shown that the selected coupled (C1, C2 and C3) suspension configurations could offer enhanced properties in roll, pitch and warp modes, and greater potential for decoupling among different modes [9]. The relative performance potentials of the coupled suspension configurations are further evaluated in terms of directional responses to braking and steering inputs. The equations of motion for the full-vehicle model equipped with different suspension configurations are analyzed through simultaneous solutions of Equations (1) to (4), together with the dynamic strut forces presented in [9]. The parameters of the vehicle model and selected suspension configurations are identical to those reported in the first part of the study [9].

The relative roll and pitch dynamic responses of the vehicle model with coupled and uncoupled configurations were evaluated for two critical maneuvers, namely braking-in-a-turn and split-μ straight-line braking [3, 22, 27]. Two road surfaces with different friction characteristics were considered for the analyses: (i) a dry road with adhesion coefficient of 0.9, referred to as ‘dry surface’; and (ii) a wet road with adhesion coefficient of 0.5, referred to as ‘wet surface’ [28]. The initial vehicle speed for the analyses was selected as 28 m/s, while the braking torque distribution was selected to be proportional to the static weight distribution between the two axles of the vehicle [29].

Accurate modeling of vehicle braking torque has been extremely difficult due to the complexities associated with the brake-fade effect [29, 30]. The constant braking torque with a transient response in the absence of brake fade, therefore, has been generally utilized to provide a first-order approximation [29-32]. A novel braking torque model was proposed in an attempt to account for the brake fade effect [33]:

$$T_b = b_1 \left\{ e^{-\left[b_5(t-b_7/2)\right]^{b_3}} - b_2 e^{-\left[b_6(t-b_8/2)\right]^{b_4}} \right\} \tag{5}$$

where T_b is braking torque, and b_i (i=1,2,…,8) are constant parameters determining the variations in the braking torque. Figure 3 illustrates the braking torque and steer angle inputs applied during the braking-in-a-turn maneuver. The analysis corresponding to split- μ straight-line braking maneuver were performed assuming adhesion coefficients of 0.9 and 0.5 at the left and right axle tires, respectively. Figure 4 illustrates the front and rear braking-torque inputs for the split-μ straight-line braking maneuver.

FIGURE 3

FIGURE 4

The vehicle dynamic responses under the braking-in-a-turn input are evaluated in terms of: (i) roll performance measures: sprung mass roll angle and rate; (ii) pitch performance measures: sprung mass pitch angle and rate; and (iii) handling or directional performance measures: yaw rate, lateral acceleration and vehicle path [2-4]. The vehicle responses during the split-μ straight-line braking are evaluated in terms of the above roll and pitch performance measures.

3. Results and Discussions

3.1 Vehicle Model Validation

The validity of the nonlinear 14-DOF full-vehicle model was examined using the available measured data reported in [22, 26] for a straight truck with 4.83 m wheelbase under two different maneuvers: a constant-speed steady-turn and a braking-in-turn maneuver. The data during the steady-turn tests were acquired under a constant speed, while the drive torque was applied only when it was necessary to maintain the constant vehicle speed. The simulation model was evaluated under the same steady-turn maneuver, although no drive torque was applied, while the reported test vehicle parameters were adapted in the model. The vehicle speed in the simulation thus decreased slowly during the maneuver, partly due to dissipation of some of the kinetic energy through suspension and tire damping. The simulations were thus performed with a slightly higher initial vehicle speed than that reported for the field tests, while the mean of the reported steer angles was applied to the front wheels. The lateral acceleration and yaw rate responses of the simulation model were extracted when the vehicle speed approached the field-test speed.

In the braking-in-a-turn maneuver tests, a constant forward speed was maintained until the steady-state responses were attained [22]. A braking input was subsequently applied with a delay of 2 s following the condition of steady-state lateral acceleration response. Subsequently, the steer angle was held unchanged until the vehicle approached its full stop. The steer angles of the left and right wheels were measured as 7˚ and 8.5˚, respectively. The model simulations were performed assuming parallel steering with

mean front wheel steer angle of 7.7°, as shown in Figure 5, while tire-road adhesion coefficient was assumed as 0.85. In the simulation model, the braking input was applied at a forward speed of 11.1 m/s and a delay of 2 s (Figure 5), which was identical to that reported in the experimental study [22].

FIGURE 5

Figures 6(a) and 6(b) illustrate comparisons of the model simulation results with the reported measured data under steady-state turning maneuvers at two different vehicle speeds (12 and 14.3 m/s), respectively. The results are presented in terms of steady-state lateral acceleration and yaw rate responses under four different steer angles. Reasonably good agreements are observed between the model responses and the measured data for both the vehicle speeds. Deviations between the two, however, are also evident under higher steer angle inputs, where the model responses are lower than the measured data. This may be partially attributed to the modeling assumption of minimal effect of the lateral and longitudinal motions/inertias of the unsprung masses, differences in the tire properties used in the simulation model and test vehicle tire data.

FIGURE 6

Figure 7 presents comparisons of the model responses to a braking-in-a-turn maneuver in terms of time-histories of lateral acceleration, longitudinal acceleration and yaw rate with the measured data. The comparisons suggest reasonably good agreements between the simulation results and the measured data. Some differences, however, can also be observed between the two, which may be partially attributed to the differences in the tire properties considered in the simulation model, and in-part to the idealized ramp-step

steering and braking inputs used in the simulation. The comparisons, presented in Figs. 6 and 7, however, demonstrate the validity of the 14-DOF vehicle model under steady-turning and braking-in-turn maneuvers considered. The model could thus be applied to study the handling and directional response characteristics of the vehicle model with fluidically-coupled suspension systems.

FIGURE 7

3.2 Responses to Braking-in-a-Turn Maneuver

Figure 8 illustrates comparisons of sprung mass roll angle and velocity responses of the vehicle model with five selected suspension configurations (C1~C3, U1 and U1bar) under the braking-in-a-turn inputs on a dry road surface (Fig. 3). The design parameters of the anti-roll bar were selected such that the static roll stiffness of U1bar suspension was identical to those of the coupled suspensions [9]. The results show that all the three fluidically-coupled suspensions (C1~C3) yield nearly identical roll responses. The peak roll angle and rate responses of the coupled suspensions, however, are considerably lower compared to those of the uncoupled suspension U1 but comparable to those of the configuration U1bar. The higher roll mode stiffness of the coupled and U1bar suspensions is also evident from the relatively higher oscillation frequency of their responses compared to the U1 configuration. Furthermore, the roll rate responses of coupled suspensions decay faster than those of the uncoupled suspension, which is attributed to the enhanced roll-mode damping properties of the fluidically-coupled suspensions. The model responses to braking-in-turn maneuver on the wet surface also revealed similar trends and are thus not presented.

Unlike the anti-roll bars, the passive fluidically-coupled suspension systems could automatically yield fluidic mass flows among different hydro-pneumatic suspension units without additional active control systems, subject to a relative roll displacement between the sprung mass and the unsprung masses. For different suspension interconnection configurations, such fluidic mass flows among different suspension units would help to generate different suspension stiffness and damping forces (and properties) under relative motions between the sprung mass and the unsprung masses, as also seen from the first part of this study. Such characteristics of the passive fluidically-coupled suspension systems thus have considerable potentials in improving vehicle dynamic performances, as evident in Fig. 8. It should be further noted that such enhancements in vehicle dynamics are realized in an energy-efficient manner without added active control systems.

FIGURE 8

Figure 9 compares the pitch angle and pitch rate responses of the sprung mass of the vehicle model with the five selected suspension configurations under the defined braking-in-a-turn inputs on a dry road surface. The results clearly show that all of the fluidically-coupled suspension configurations (C1~C3) yield significantly lower peak pitch angle and rate, when compared to those with uncoupled suspensions (U1 and U1bar). Furthermore, the hybrid coupled suspension involving hydraulic and pneumatic couplings (C3) yields lower magnitudes of pitch responses compared to pneumatically-coupled configuration (C2), while hydraulically-coupled configuration (C1) yields lowest magnitudes of pitch responses. This is attributed to the higher pitch-mode stiffness and damping of the hydraulically-coupled C1 configuration [9]. The use of anti-roll bars, as expected, cannot provide improvements in the pitch

responses.

FIGURE 9

For light vehicles with independent suspensions, suspension kinematics can be synthesized to inhibit pitch motions. The geometry of such anti-pitch suspension designs, however, tends to induce greater wheel hop and adversely affect the handling dynamics of the vehicle [34, 35]. The heavy vehicle suspension designs generally employ a load equalizing mechanism to realize even axle load distribution in a tandem axle arrangement. Unequal load distributions and thus appreciable pitch motions, however, are known to occur during braking and acceleration [26, 36]. The realization of anti-pitch characteristics of road vehicle suspensions, particularly for heavy vehicles, thus continues to be a very challenging design task. The results presented in Figs. 8 and 9 suggest that the fluidically-coupled hydro-pneumatic suspension struts could conveniently yield improved anti-roll as well as anti-pitch properties.

Figure 10 compares the directional responses of the vehicle model with different suspension configurations in terms of lateral acceleration, yaw rate and the vehicle path during the defined braking-in-a-turn maneuver on a dry surface. The results show that the yaw rate and lateral acceleration responses of the model with fluidically-coupled (C1~C3) and U1bar suspension configurations are slightly lower those of the model with unconnected U1 suspension. The coupled and U1bar suspensions thus cause slightly larger turning radius. The results therefore suggest a slightly higher understeer tendency of the coupled suspensions, which is considered to be beneficial in view of the directional stability limit during emergency-type steering maneuvers [2, 4].

FIGURE 10

3.3 Responses to Split-μ Straight-Line Braking

The sprung mass roll angle and roll rate responses of the vehicle model with the selected suspensions to the defined split-μ straight-line braking inputs (Fig. 4) are compared in Fig. 11, while Fig. 12 illustrates the pitch angle and pitch rate responses. The results show that all the three fluidically-coupled suspension configurations (C1~C3) yield lower magnitudes of roll and pitch deflections and rates of the sprung mass, compared to unconnected suspension (U1), as observed under the braking-in-a-turn maneuver. While the U1bar suspension also yields sprung mass roll response comparable to those of the coupled suspensions, its pitch angle response is nearly identical that of the U1 suspension. The results thus further confirm the improved anti-roll and anti-pitch properties of the proposed fluidically-coupled suspension systems, which could provide enhanced handling and directional stability and control performances.

FIGURE 11

FIGURE 12

3.3 Ride Vibration Responses

The measured road roughness data of three different roads in Quebec (Canada) are considered for relative ride dynamic analyses of different suspension configurations [37]. The measured data of road elevations consisted of both the roughness variations

and the local road gradients of the left and right tracks. The contributions due to low-frequency variations associated with changes in the local gradients are often attenuated by using a high-pass filter. A high pass filter with a cut-off frequency 0.3 Hz was applied to eliminate the contributions due to local gradients in elevations [37]. The filtered roughness data of the selected three road profiles were used for the dynamic analyses. Figure 13 illustrates the vertical displacement and acceleration temporal power spectral density (PSD) characteristics of the three road profiles at a forward speed of 70 km/h. The displacement PSD characteristics of the selected three roads exhibit trends similar to those reported in [4, 14, 38]. On the basis of their relative displacement PSD characteristics, the selected three roads are referred to as '*smooth*', '*medium-rough*' and '*rough*', as illustrated in Figs. 13(a), (b) and (c), respectively.

FIGURE 13

Vehicle model is analyzed to derive the ride responses in terms of vertical acceleration of the sprung mass and vertical suspension travel. Owing to the comparable properties of the three coupled suspension configurations, the ride response of the model with coupled suspension are evaluated for configuration C1 only. The vertical ride vibration responses of the vehicle model with three different suspensions (C1, U1 and U1bar) are evaluated under excitations arising from the three random road surfaces and different vehicle speeds (30, 50, 70, 90 and 110 km/h). Human perception of ride comfort related to vertical vibration has been associated with root mean square (rms) acceleration responses [2, 4, 39]. Although the assessment of human perception of ride vibration requires the use of frequency-weighted rms acceleration levels at the human seat interface as defined in ISO-2631-1 [39], the relative vertical ride perceptions of different suspension configurations can be effectively evaluated from the rms values of

the un-weighted rms vertical acceleration response of the sprung mass.

Figure 14 compares the rms vertical acceleration values of the sprung mass of the vehicle model employing three different suspension configurations (C1, U1 and U1bar). The results show that configurations U1 and U1bar yield comparable vertical ride responses for most of road conditions and vehicle speeds considered. The fluidically-coupled suspension C1, however, yields lower values of rms sprung mass vertical acceleration, irrespective of the road surface irregularity and forward speed. The results suggest the additional potential benefit of the fluidic-couplings of suspension units in view of the vertical ride. It should be noted that the parameters of the coupled suspension configuration were chosen to yield bounce-mode stiffness and damping properties identical to those of the U1 and U1bar suspensions [9]. The reduced vertical ride response of the coupled suspension is most likely attributed to its enhanced vehicle attitude control and thus reduced coupled oscillations among the bounce, roll and pitch modes of the sprung mass.

FIGURE 14

Suspension design and tuning of road vehicles are constrained by available rattle space [4]. A relatively larger suspension travel would tend to increase the possibility of impacts against the rebound/bump stops resulting in poor ride quality and unexpected handling characteristic. Figures 15 and 16, as examples, present the rms and peak suspension travel responses of the front-left and rear-right suspension units of the vehicle, respectively. The results show that configurations U1 and U1bar yield comparable front suspension travel responses under the road roughness and driving

speed conditions considered in the analysis. The fluidically-coupled suspension C1, however, yields considerably lower magnitudes of front suspension travel, compared to the unconnected suspension with and without anti-roll bars (U1bar and U1) for all the road roughness and forward speeds considered. This improvement in front suspension travel is highly desirable, considering the design challenges associated with front wheels suspension design for a front-wheel-steering vehicle. A lower magnitude of front suspension travel would minimize the undesirable coupling effect between the front suspension and the steering systems. The results suggest that the rear suspension travel responses are strongly affected by the road roughness and the driving speed. The results, presented in Fig. 16, do not show a clear response trend for the three suspension configurations investigated. At relatively lower speeds, configuration C1 tends to yield lower magnitudes of rear suspension travels, but at relatively higher speeds, such trend cannot be observed. The results, however, suggest that the fluidically-interconnected would yield an overall improvement in the suspension travel responses, while the use of anti-roll bars cannot help enhance the suspension travel.

FIGURE 15

FIGURE 16

3.4 Sensitivity to Variations in a Suspension Design Parameter

The superior design flexibility of fluidically-interconnected suspension has been

demonstrated in the first part of the study [9]. It was shown that an increase of 20% in the annular piston area of the front suspension struts would yield higher suspension roll and pitch stiffness, while retaining the lower vertical mode stiffness for preserving vibration the ride quality. The dynamic responses of the vehicle model are further evaluated by considering 20% larger annular piston area of the hydraulically-coupled suspension, referred to as configuration C1r, to investigate the potential performance gain. The vehicle model responses to braking-in-a-turn and split-μ straight-line braking maneuvers are evaluated and compared to those of the vehicle with the nominal C1 suspension configuration.

Figure 17 presents the sprung mass roll and pitch dynamic responses of the vehicle with the two suspension configurations (C1 and C1r) to selected braking-in-a-turn inputs on the dry surface (Fig. 3). The results show that configuration C1r yields lower magnitudes of the sprung mass roll and pitch angle responses compared to those of the vehicle with configuration C1. These are attributed to enhanced roll- and pitch-mode stiffness properties of the modified C1r suspension. The relative directional responses of the vehicle with the two suspensions in terms of yaw rate, lateral acceleration and vehicle path during the defined braking-in-a-turn maneuver on a dry surface revealed only slight increase in the understeer tendency (the results are not presented here).

FIGURE 17

Figures 18(a) and (b) illustrate the sprung mass roll and pitch responses to defined split-μ straight-line braking inputs (Fig. 4), respectively. The results show that configurations C1r, involving a 20% larger front suspension annular piston area, yields

lower magnitudes of the roll and pitch deflections of the sprung mass. The results are consistent with the anti-roll and anti-pitch properties analyzed in the first part of the study [9].

FIGURE 18

Table 2 compares the different ride dynamic responses of the vehicle model with the nominal and modified hydraulically coupled suspension configurations (C1 and C1r) corresponding to two different forward speeds: 50 and 90 km/h The ride measures were obtained for the *smooth* road roughness inputs. The results suggest quite comparable responses of the two suspension configurations for the two speeds considered. The results presented in Figs. 17 and 18, and Table 2 suggest that the use of a larger front suspension annular piston area tends to help improve anti-roll and anti-pitch characteristics, with only minimal influence on the vehicle vertical ride and suspension travel responses. This further confirms the superior design and design flexibility of fluidically-interconnected suspension system.

TABLE 2

4 Conclusions

This second part of the study investigated the potential benefits of fluidically-coupled suspension systems on vehicle ride, handling, roll and pitch dynamic responses under various road excitations and braking and/or steering maneuvers. The dynamic responses

of the proposed coupled and uncoupled suspension strut arrangements were evaluated using a generalized and validated 14-DOF nonlinear model of two-axle road vehicles. The roll, pitch and handling performance measures were assessed under two critical handling maneuvers: braking-in-a-turn and split-μ straight-line braking. The ride and suspension travel responses were further evaluated under a range of measured road roughness profiles and vehicle speeds.

The simulation results demonstrated that the proposed full-vehicle coupled hydro-pneumatic suspension systems could yield considerably enhanced anti-roll and anti-pitch properties, handling performance, roll and directional stability limits, as well as improved vertical primary ride and suspension travel responses of road vehicles. The benefits of design parameter tuning of fluidically-coupled suspension were further shown. The systematic analyses of feasibility, suspension properties, design sensitivity, and vehicle dynamic responses clearly demonstrated the considerable potential of fluidically-interconnected hydro-pneumatic suspension in enhancing overall vehicle ride and handling performance and driving stability in an energy-saving manner, apart from its superior design and tuning flexibility.

References

1. Kang, X., Rakheja, S. and Stiharu, I., 2001, 'Effects of tank shape on the roll dynamic response of a partly filled tank vehicle', Vehicle System Dynamics, 35, p.75-102.

2. Cole, D.J., 2001, 'Fundamental issues in suspension design for heavy road vehicles', Vehicle System Dynamics, 35, p.319-360.
3. Dahlberg, E., 1999, 'Yaw instability due to longitudinal load transfer during braking in a curve', SAE paper 1999-01-2952.
4. Wong, J.Y., 2001, 'Theory of ground vehicles', 3rd Edition, John Wiley & Sons, Inc., USA.
5. Sharp, R.S., 1999, 'Vehicle dynamics and the judgment of quality', Vehicle Performance, Edited by Pauwelussen, J.P., Swets & Zeitlinger Publishers, Lisse, the Netherlands, p.87-96.
6. Cao, D., Rakheja, S. and Su, C.-Y., 2008, 'Heavy vehicle pitch dynamics and suspension tuning. Part I: Unconnected suspension'. Vehicle System Dynamics, 46, p.931-953.
7. Williams, R.A., 1997, 'Automotive active suspensions. Part 2: practical considerations', Journal of Automobile Engineering, 211, p.427-444.
8. Rajamani, R., 2006, 'Vehicle dynamics and control', Springer, NY, USA.
9. Cao, D., Rakheja, S. and Su, C.-Y., 'Roll- and pitch-plane coupled hydro-pneumatic suspension. Part 1: Feasibility analysis and suspension properties', Vehicle System Dynamics. (Under review)
10. Hegazy, S., Rahnejat, H. and Hussain, K., 2000, 'Multi-body dynamics in full-vehicle handling analysis under transient manoeuver', Vehicle System Dynamics, 34, p.1-34.
11. Savkoor, A.R., Happel, H. and Horkay, F., 1999, 'Vehicle handling and sensitivity in transient maneuvers', Vehicle Performance, Edited by Pauwelussen, J.P., Swets & Zeitlinger Publishers, Lisse, the Netherlands, p.121-147.

12. El-Gindy, M. and Wong, J.Y., 1987, ‘A comparison of various computer simulation models for predicting the directional responses of articulated vehicles’, Vehicle System Dynamics, 16, p.249-268.
13. Ervin, R.D., 1986, ‘The dependence of truck roll stability on size and weight variables’, International Journal of Vehicle Design, 7, p.192-208.
14. Cebon, D., 1999, ‘Handbook of vehicle-road interaction’, Swets & Zeitlinger, the Netherlands.
15. Giangiulio, E., 2006, ‘14 d.o.f. VERTEC vehicle model VDSIM – Vehicle Dynamic SIMulator Implementation and validation’, 3rd International Colloquium on Vehicle-Tyre-Road Interaction, Stuttgart, Germany.
16. Shim, T. and Ghike, C., 2007, ‘Understanding the limitations of different vehicle models for roll dynamics studies’, Vehicle System Dynamics, 45, p.191-216.
17. Cole, D.J., 2000, ‘Evaluation of design alternatives for roll-control of road vehicles’, Proceedings of AVEC 2000, Ann Arbor, USA.
18. Sampson, D.J.M. and Cebon, D., 2003, ‘Active roll control of single unit heavy road vehicles’, Vehicle System Dynamics, 40, p.229-270.
19. Blundell, M.V., 2000, ‘The modelling and simulation of vehicle handling. Part 3: tyre modelling’, Journal of Multi-Body Dynamics, 214, p.1-32.
20. Pacejka, H.B., 2002, ‘Tire and vehicle dynamics ’, SAE Inc., PA, USA.
21. Cao, D., Rakheja, S. and Su, C.-Y., 2006, ‘A generalized model of a class of interconnected hydro-pneumatic suspensions and analysis of pitch properties’, Proc. of ASME Int. Mech. Engineering Congress, IMECE2006-13961, Chicago, USA.
22. Bernard, J.E. Winkler, C.B. and Fancher, P.S., 1973, ‘A computer based mathematical method for predicting the directional response of trucks and tractor-trailers’, UMTRI Technical Report UM-HSRI-PF-73-1, The University of Michigan, USA.

23. Klasson, J., 2002, ‘A generalized crosswind model for vehicle simulation purposes’, Vehicle System Dynamics Supplement, 37, p.350-359.
24. Bakker, E., Byborg, L. and Pacejka, H.B., 1987, ‘Tyre modeling for use in vehicle dynamic studies’, SAE paper 870421.
25. Pacejka, H.B. and Bakker, E., 1991, ‘The magic formula tyre model’, Proc. of 1st Tyre Colloquium, Delft, The Netherland.
26. Murphy, R.W., Bernard, J.E. and Winkler, C.B., 1972, ‘A computer based mathematical method for predicting the braking performance of trucks and tractor-trailers’, UMTRI Report UM-HSRI-PF-72-1, The University of Michigan, USA.
27. Data, S. and Frigerio, F., 2002, ‘Objective evaluation of handling quality’, Journal of Automobile Engineering, 216, p.297-305.
28. Fancher, P.S., 1995, ‘Generic data for representing truck tire characteristics in simulations of braking and braking-in-a-turn maneuvers’, UMTRI Report 95-34, The University of Michigan, USA.
29. Fancher, P.S., Ervin, R.D., Winkler, C.B. and Gillespie, T.D., 1986, ‘A factbook of the mechanical properties of the components for single-unit and articulated heavy trucks’, UMTRI Report UMTRI-86-12, The University of Michigan, USA.
30. Winkler, C.B., Bernard, J.E., Fancher, P.S., Macadam, C.C. and Post T.M., 1976, ‘Predicting the braking performance of trucks and tractor-trailers’, UMTRI Report UM-HSRI-76-26-1, The University of Michigan, USA.
31. Suh, M.-W., Park, Y.-K., Kwon, S.-J., Yang, S.-H. and Park, B.-C., 2000, ‘A simulation program for the braking characteristics of tractor-semitrailer vehicle’, SAE paper 2000-01-3415.

32. Kaneko, T., Kageyama, I. and Tsunashima, H., 2002, 'Braking stability of articulated vehicles on highway', Vehicle System Dynamics Supplement, 37, p.1-11.
33. Cao, D., Rakheja, S. and Su, C.-Y., 'Dynamic analyses of heavy vehicle with pitch-interconnected suspensions', International Journal of Heavy Vehicle Systems. (In press)
34. Dixon, J.C., 1996, 'Tires, suspension and handling', 2nd Edition, SAE Inc., PA, USA.
35. Sharp, R.S., 1999, 'Influence of suspension kinematics on pitching dynamics of cars in longitudinal maneuvering', Vehicle System Dynamics Supplement, 33, p.23-36.
36. Timoney, E.P. and Timoney, S.S., 2003, 'A review of the development of independent suspension for heavy vehicles', SAE paper 2003-01-3433.
37. Rakheja, S., Wang Z. and Ahmed A.K.W., 2001, 'Urban bus optimal passive suspension study. Phase II: Enhancement of road- and driver-friendliness of urban buses through optimal suspension damping', Transportation Canada Report T-8200-4-4556, Canada.
38. Gillespie, T.D., 1985, 'Heavy truck ride', SAE paper 850001.
39. ISO 2631-1, 1997, 'Mechanical vibration and shock-Evaluation of human exposure to whole-body vibration-Part 1: General requirements', International Organization of Standardization.

Table 1: The motions of the generalized two-axle vehicle model.

Motion	Description
u	longitudinal velocity of the sprung mass
v	lateral velocity of the sprung mass
w	bounce velocity of the sprung mass
p	roll velocity of the sprung mass
q	pitch velocity of the sprung mass
r	yaw velocity of the sprung mass
z_{uf}, z_{ur}	bounce displacements of the front and rear unsprung masses, respectively
θ_{uf}, θ_{ur}	roll angles of the front and rear unsprung masses, respectively
ω_{fl}, ω_{fr}, ω_{rl}, ω_{rr}	angular velocities of the front-left, front-right, rear-left and rear-right wheels, respectively

Table 2: Performance comparison between configurations C1 and C1r under *smooth* road inputs.

Measure	C1	C1r
50 km/h		
Rms sprung mass bounce acceleration (m/s^2)	0.154	0.159
Rms front-left suspension travel (m)	0.0021	0.0021
Rms front-right suspension travel (m)	0.0022	0.0021
Rms rear-left suspension travel (m)	0.0019	0.0019
Rms rear-right suspension travel (m)	0.002	0.002
Peak front-left suspension travel (m)	0.0059	0.0055
Peak front-right suspension travel (m)	0.0058	0.0055
Peak rear-left suspension travel (m)	0.0054	0.0054
Peak rear-right suspension travel (m)	0.0056	0.0056
90 km/h		
Rms sprung mass bounce acceleration (m/s^2)	0.241	0.232
Rms front-left suspension travel (m)	0.0023	0.0022
Rms front-right suspension travel (m)	0.0026	0.0024
Rms rear-left suspension travel (m)	0.0031	0.003
Rms rear-right suspension travel (m)	0.0033	0.0033
Peak front-left suspension travel (m)	0.0065	0.0061
Peak front-right suspension travel (m)	0.007	0.0067
Peak rear-left suspension travel (m)	0.0077	0.0077
Peak rear-right suspension travel (m)	0.0078	0.0077

Fig. 1: (a) Representation of a 14-DOF two-axle vehicle model; and (b) forces and moments acting on a wheel and tire assembly under braking.

Fig. 2: The selected coupled and unconnected hydro-pneumatic suspension configurations.

Fig. 3: Representations of the idealized braking-in-a-turn inputs: (a) braking torques; and (b) steer angle.

Fig. 4: Representations of the split-μ straight-line braking inputs.

Fig. 5: Ramp-step steer angle and braking inputs corresponding to braking-in-a-turn maneuver applied in the simulation model.

Fig. 6: Comparisons of lateral acceleration (Ay) and yaw rate responses of the vehicle model with the measured data reported in [22] under a steady-state turning maneuver: (a) forward speed = 12 m/s; (b) forward speed = 14.3 m/s.

Fig. 7: Comparison of full-vehicle model responses during braking-in-a-turn with the measured data reported in [22]: (a) lateral acceleration; (b) longitudinal acceleration; and (c) yaw rate.

Fig. 8: Dynamic roll responses of the vehicle with different suspension systems under a braking-in-a-turn maneuver on the dry surface: (a) sprung mass roll angle; and (b) sprung mass roll velocity.

Fig. 9: Dynamic pitch responses of the vehicle with different suspension systems under a braking-in-a-turn maneuver on the dry surface: (a) sprung mass pitch angle; and (b) sprung mass pitch velocity.

Fig. 10: Directional responses of the vehicle with different suspension systems under a braking-in-a-turn maneuver on the dry surface: (a) lateral acceleration; (b) yaw rate; and (c) vehicle path.

Fig. 11: Dynamic roll responses of the vehicle with different suspension systems under split-μ straight-line braking: (a) sprung mass roll angle; and (b) sprung mass roll velocity.

Fig. 12: Dynamic pitch responses of the vehicle with different suspension systems under split-μ straight-line braking: (a) sprung mass pitch angle; and (b) sprung mass pitch velocity.

Fig. 13: Vertical displacement and acceleration temporal PSD characteristics of the selected three road profiles at a speed of 70 km/h: (a) *smooth*; (b) *medium-rough*; and (c) *rough*.

Fig. 14: Comparisons of the sprung mass vertical ride responses with different suspension configurations under different road conditions: (a) *smooth*; (b) *medium-rough*; and (c) *rough*.

Fig. 15: Comparisons of the front-left suspension travel with different suspension configurations under different road conditions: (a) responses under *smooth* road inputs; (b) responses under *medium-rough* road inputs; (c) responses under *rough* road inputs.

Fig. 16: Comparisons of the rear-right suspension travel with different suspension configurations under different road conditions: (a) responses under *smooth* road inputs; (b) responses under *medium-rough* road inputs; (c) responses under *rough* road inputs.

Fig. 17: Dynamic responses of the vehicle with different suspension systems under a braking-in-a-turn maneuver on the dry surface: (a) sprung mass roll angle; and (b) sprung mass pitch angle.

Fig. 18: Dynamic responses of the vehicle with different suspension systems under split-μ straight-line braking: (a) sprung mass roll angle; and (b) sprung mass pitch angle.

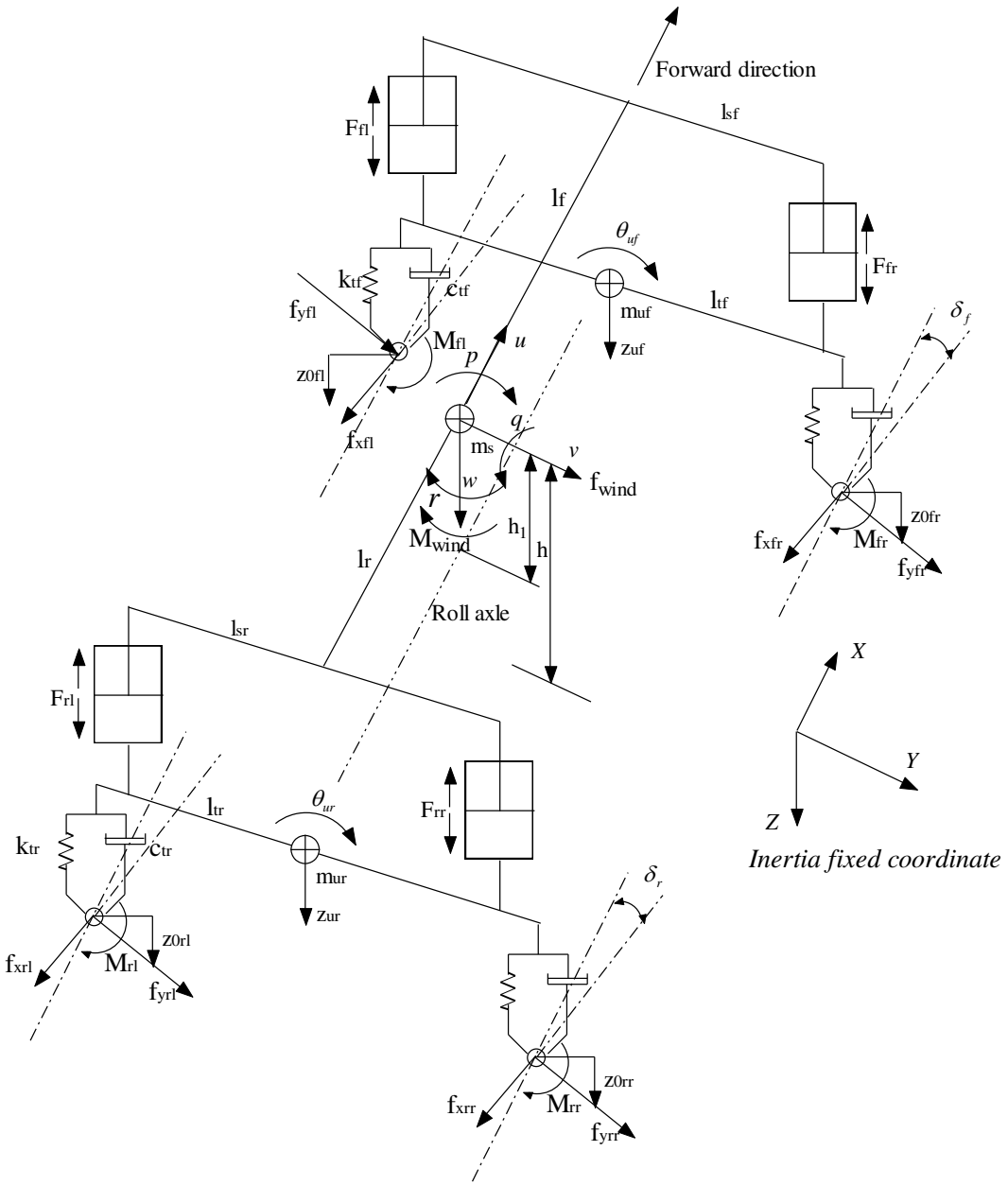

(a)

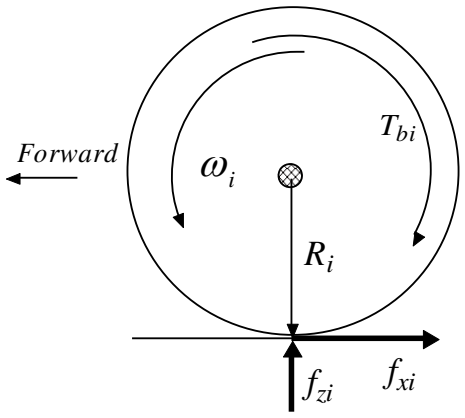

(b)

Fig. 1: (a) Representation of a 14-DOF two-axle vehicle model; and (b) forces and moments acting on a wheel and tire assembly under braking.

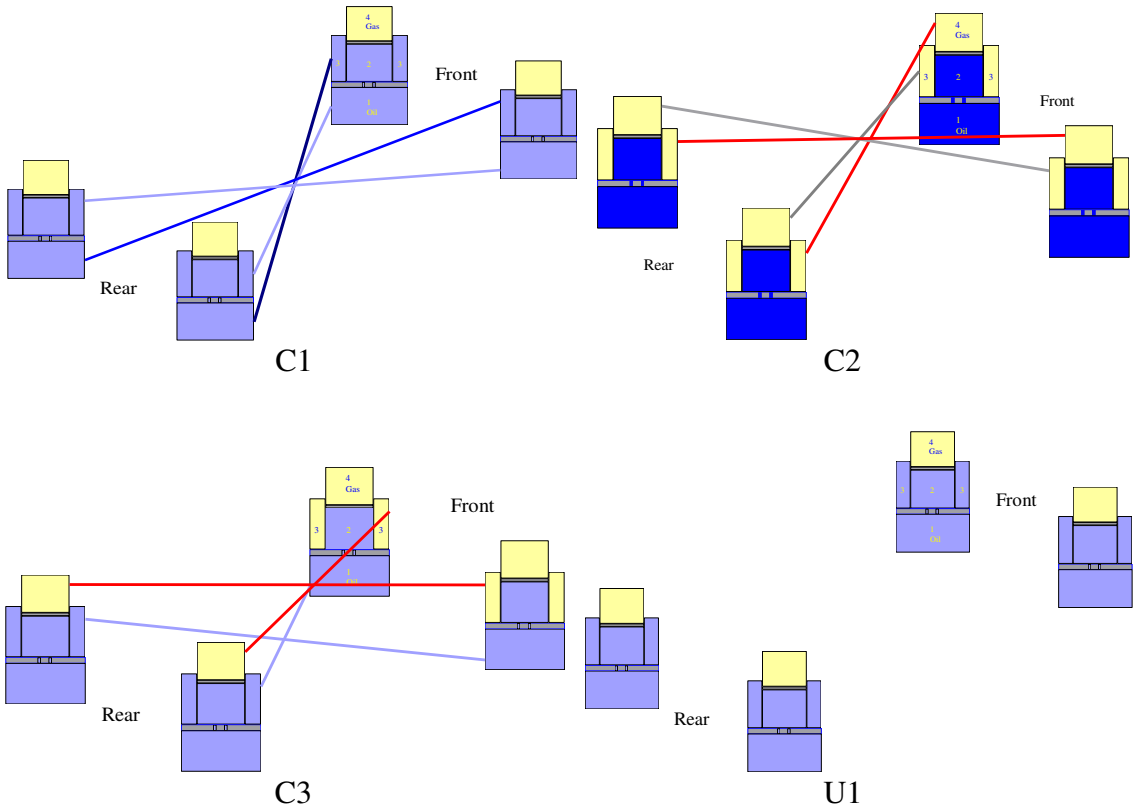

Fig. 2: The selected coupled and unconnected hydro-pneumatic suspension configurations.

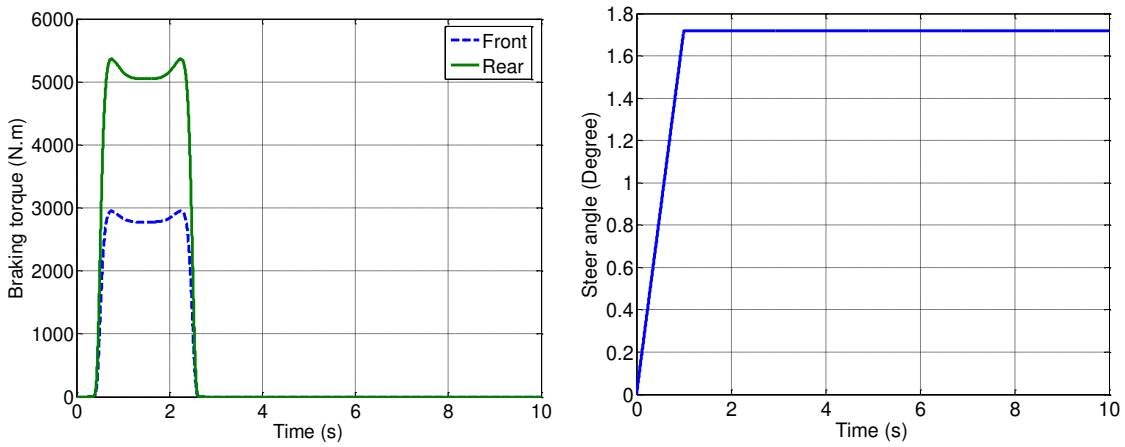

(a) (b)

Fig. 3: Representations of the idealized braking-in-a-turn inputs: (a) braking torques; and (b) steer angle.

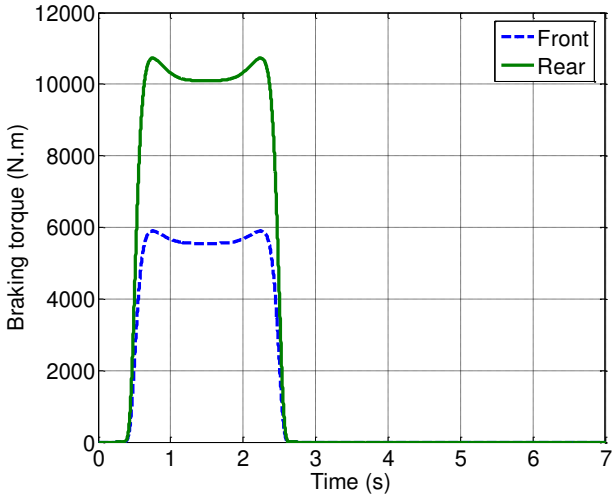

Fig. 4: Representations of the split-μ straight-line braking inputs.

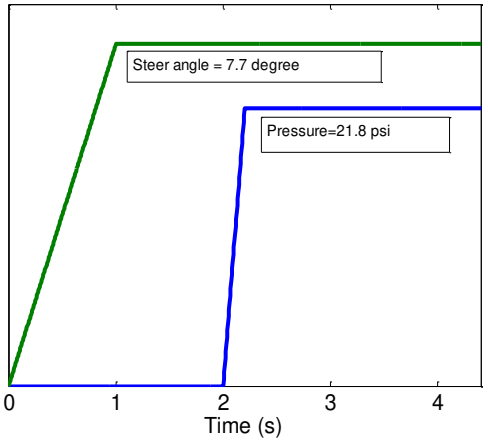

Fig. 5: Ramp-step steer angle and braking inputs corresponding to braking-in-a-turn maneuver applied in the simulation model.

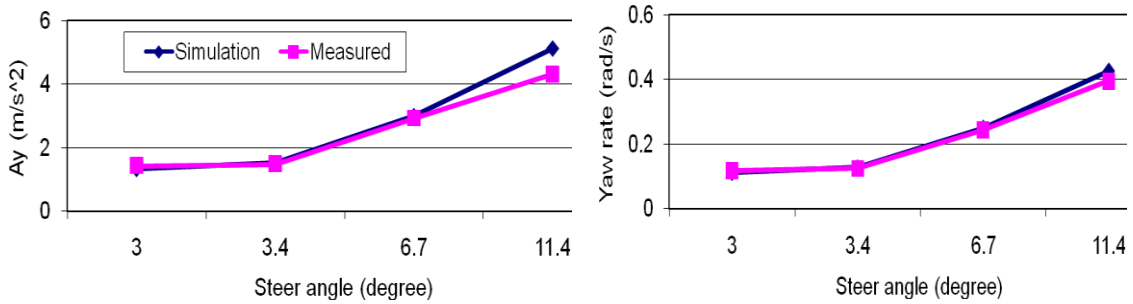

(a)

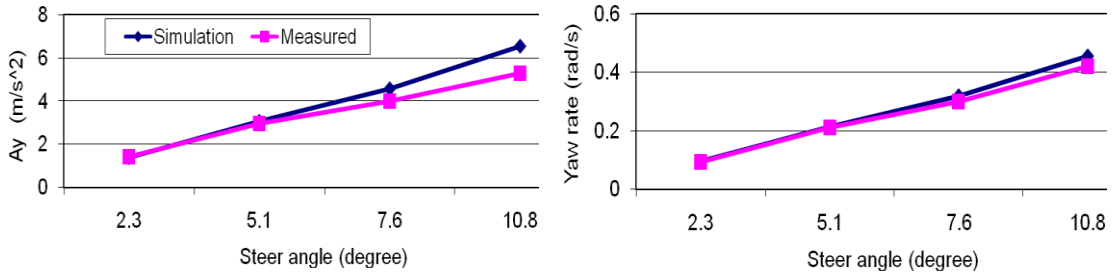

(b)

Fig. 6: Comparisons of lateral acceleration (Ay) and yaw rate responses of the vehicle model with the measured data reported in [22] under a steady-state turning maneuver: (a) forward speed = 12 m/s; (b) forward speed = 14.3 m/s.

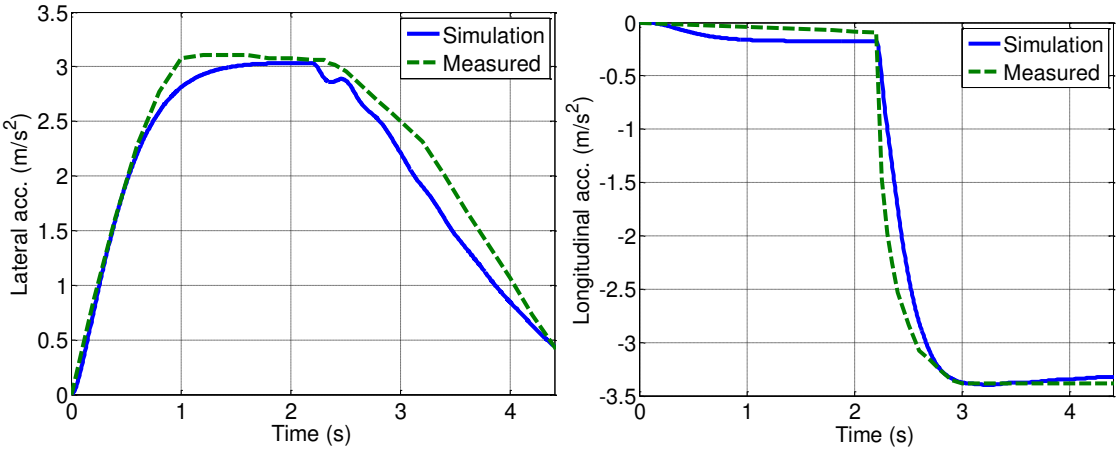

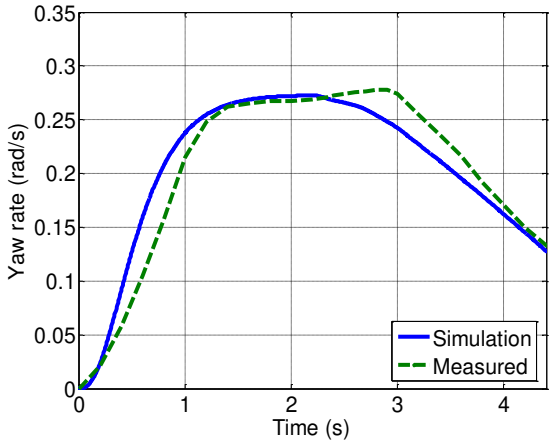

Fig. 7: Comparison of full-vehicle model responses during braking-in-a-turn with the measured data reported in [22]: (a) lateral acceleration; (b) longitudinal acceleration; and (c) yaw rate.

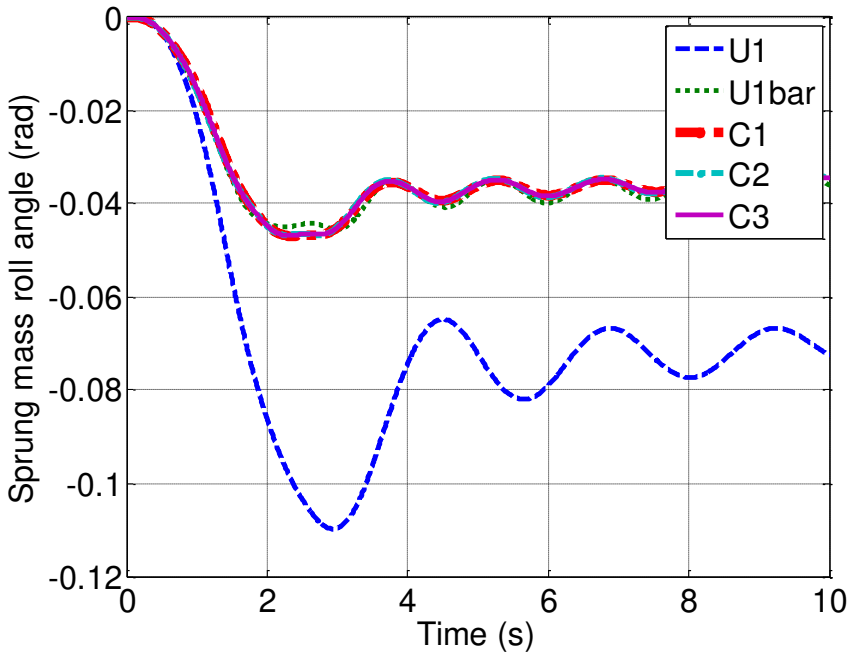

(a)

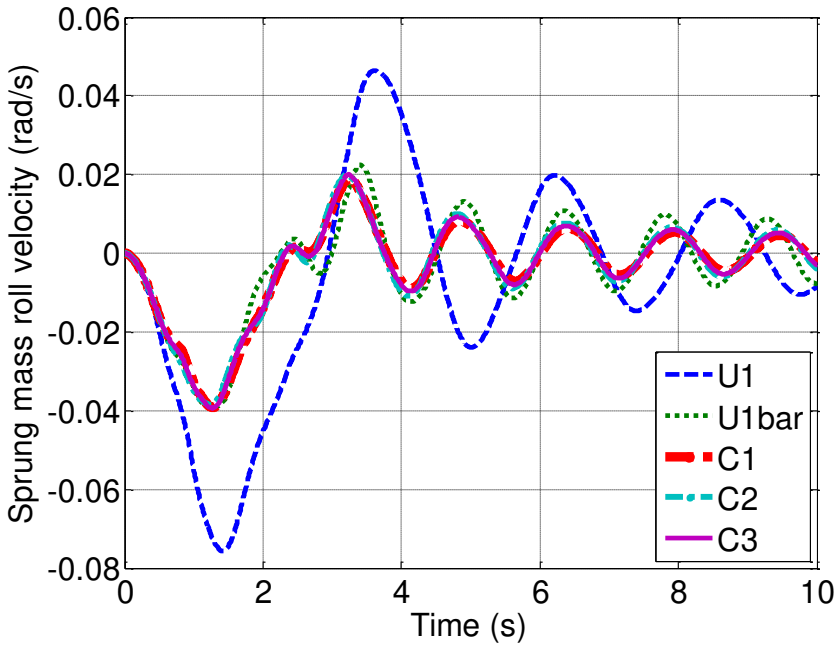

(b)

Fig. 8: Dynamic roll responses of the vehicle with different suspension systems under a braking-in-a-turn maneuver on the dry surface: (a) sprung mass roll angle; and (b) sprung mass roll velocity.

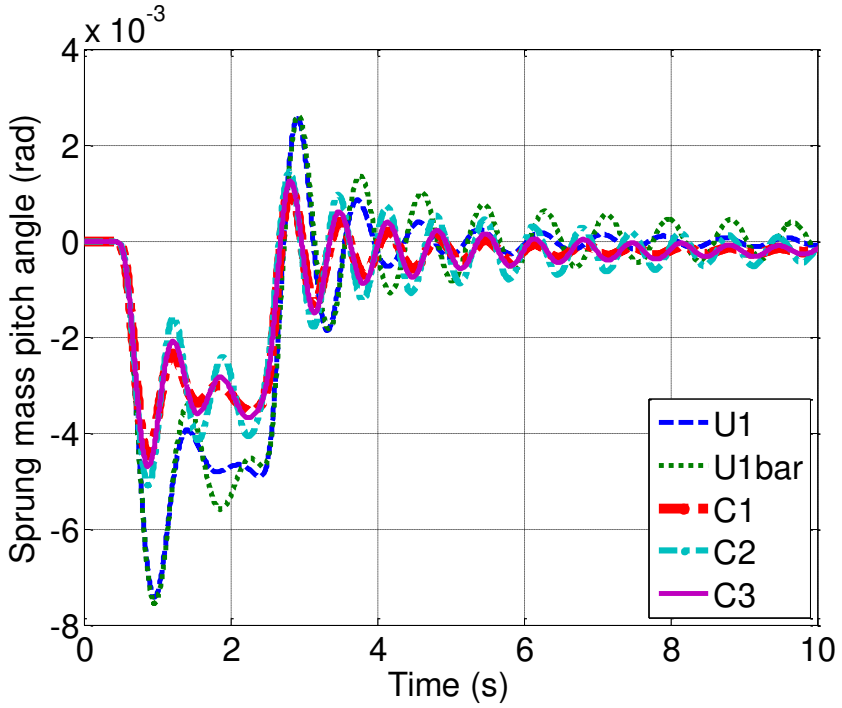

(a)

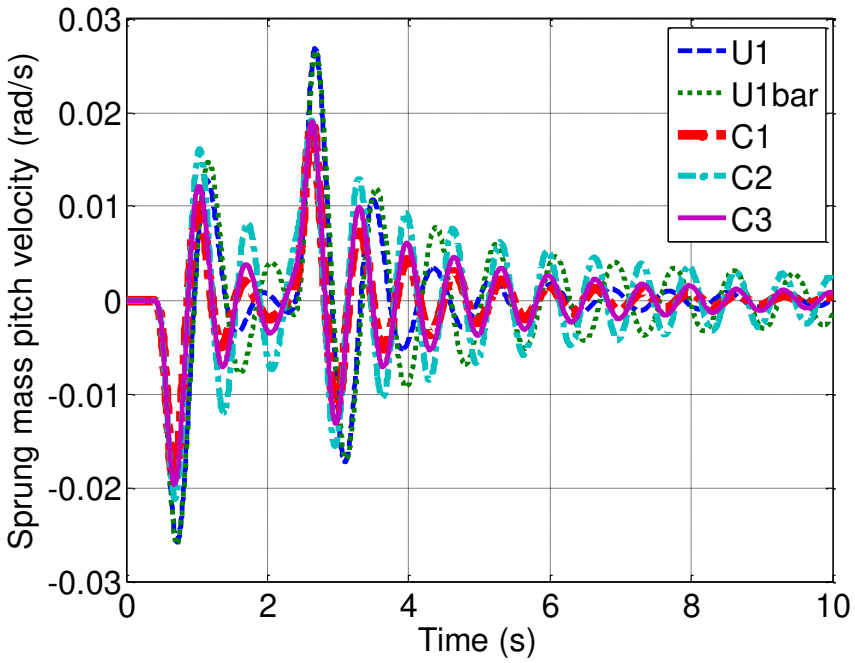

(b)

Fig. 9: Dynamic pitch responses of the vehicle with different suspension systems under a braking-in-a-turn maneuver on the dry surface: (a) sprung mass pitch angle; and (b) sprung mass pitch velocity.

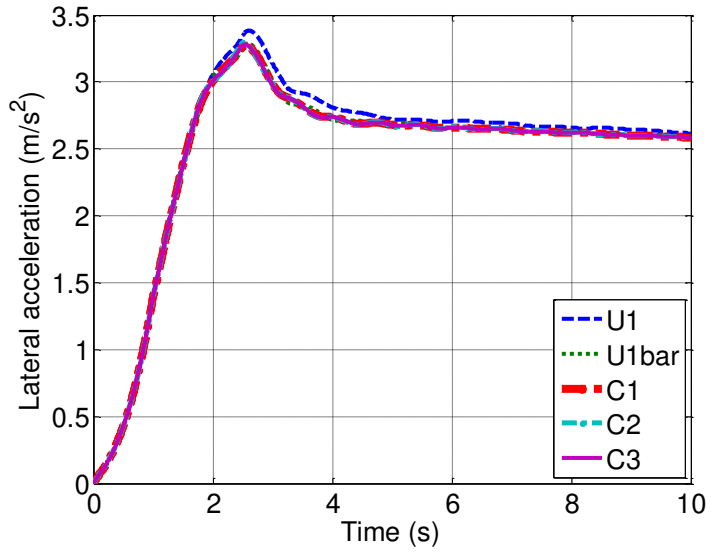

(a)

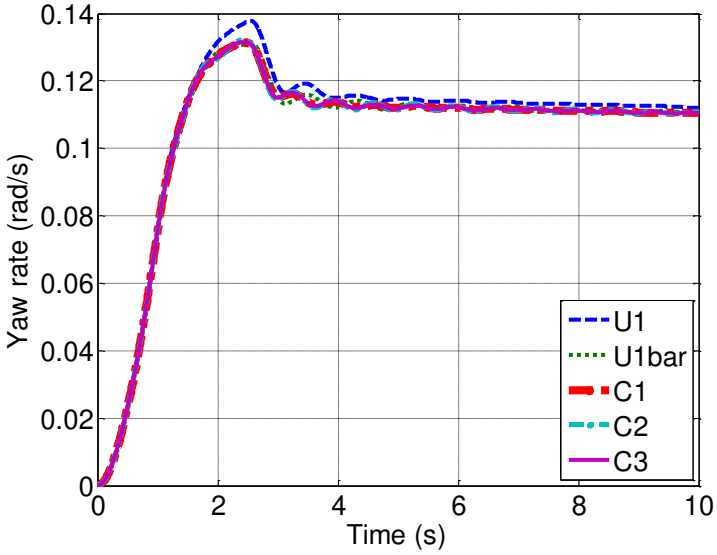

(b)

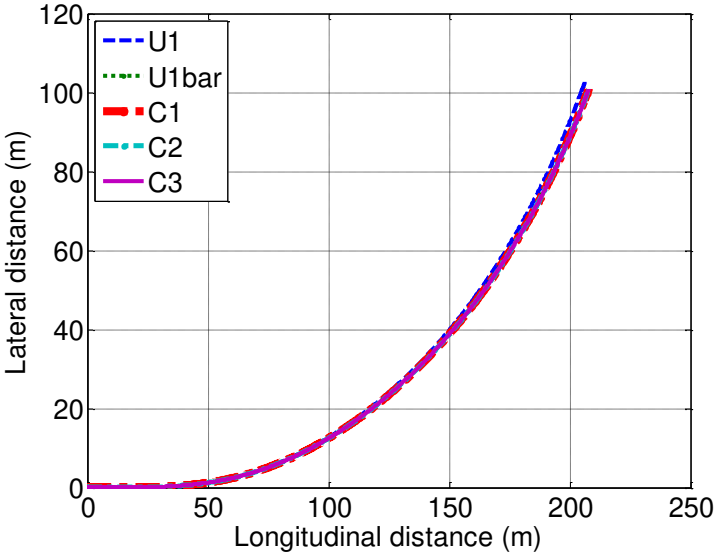

(c)

Fig. 10: Directional responses of the vehicle with different suspension systems under a braking-in-a-turn maneuver on the dry surface: (a) lateral acceleration; (b) yaw rate; and (c) vehicle path.

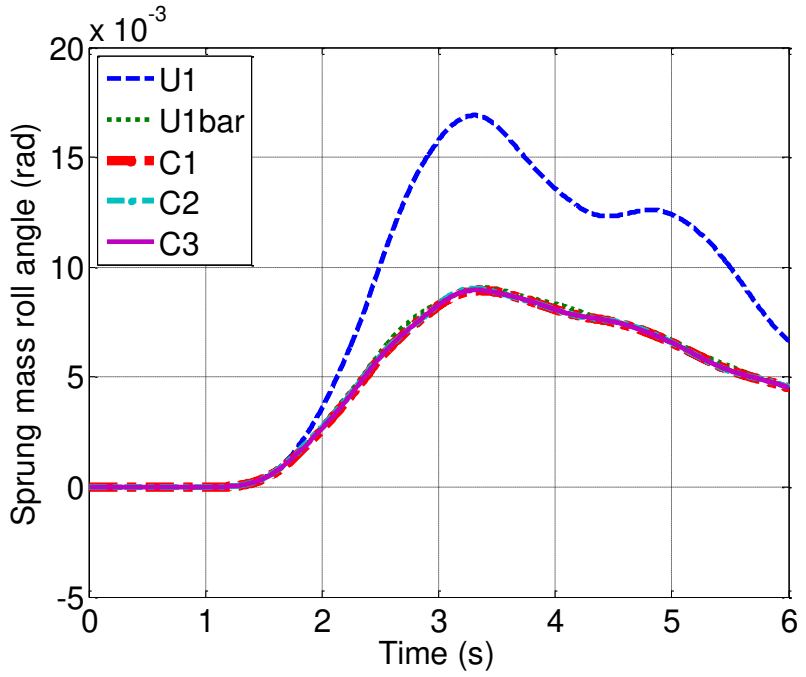

(a)

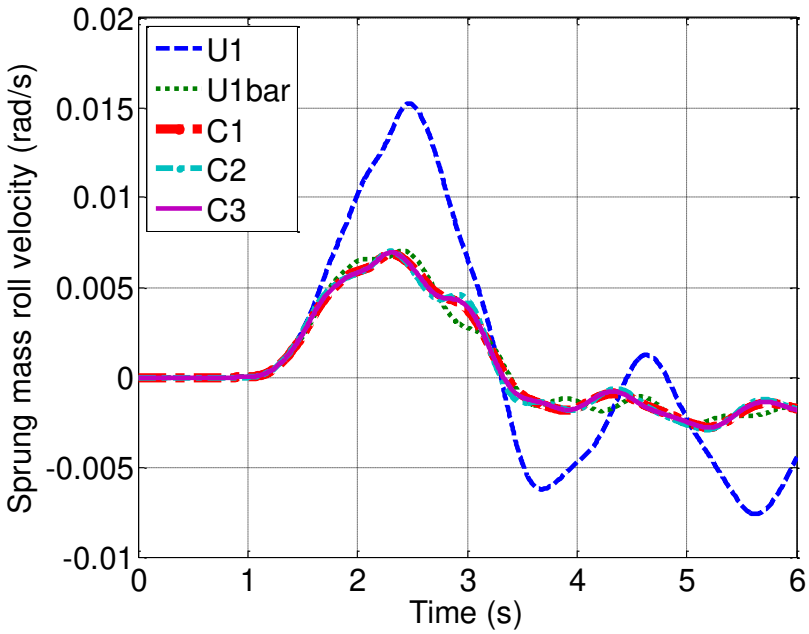

(b)

Fig. 11: Dynamic roll responses of the vehicle with different suspension systems under split-μ straight-line braking: (a) sprung mass roll angle; and (b) sprung mass roll velocity.

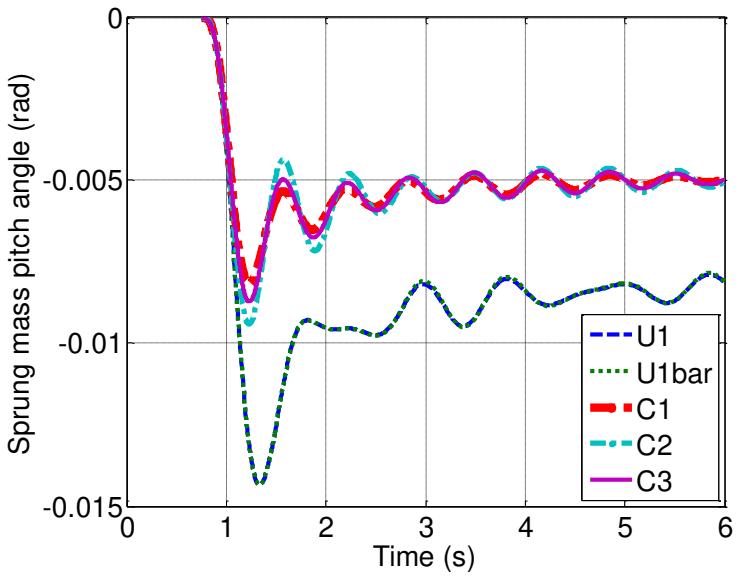

(a)

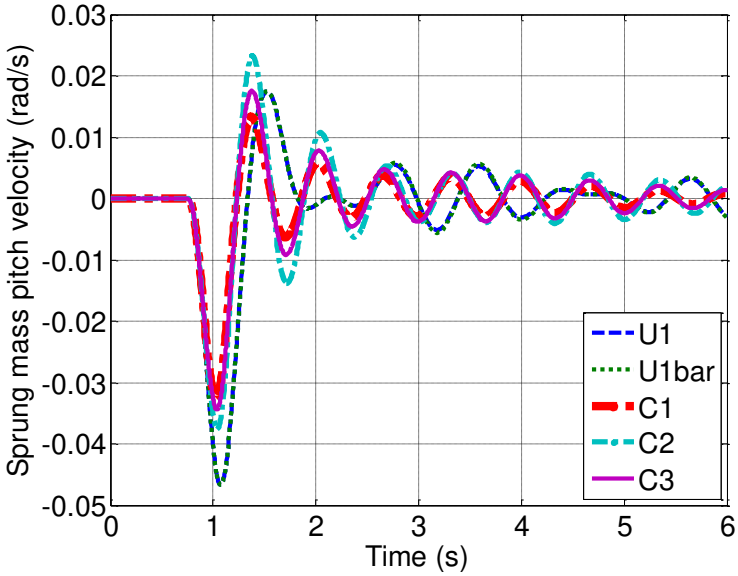

(b)

Fig. 12: Dynamic pitch responses of the vehicle with different suspension systems under split-μ straight-line braking: (a) sprung mass pitch angle; and (b) sprung mass pitch velocity.

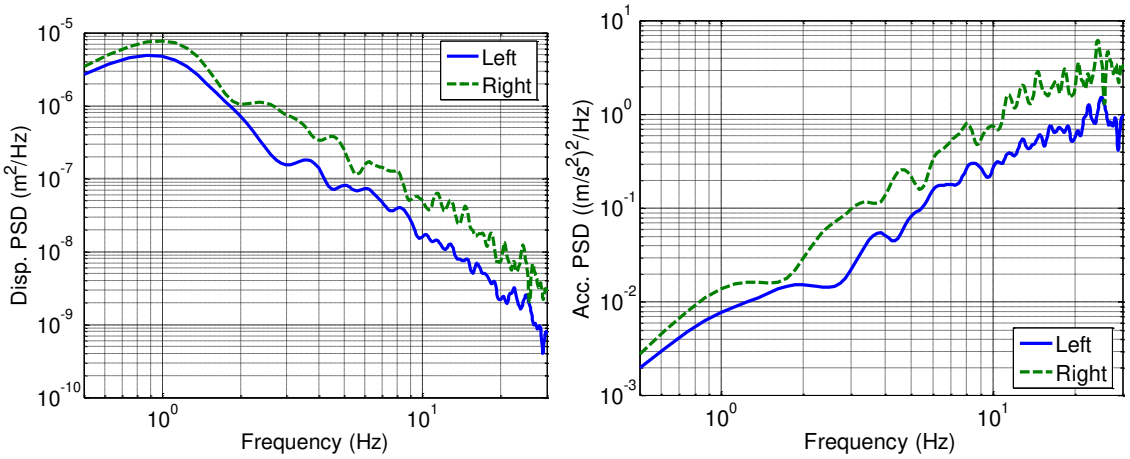

(a)

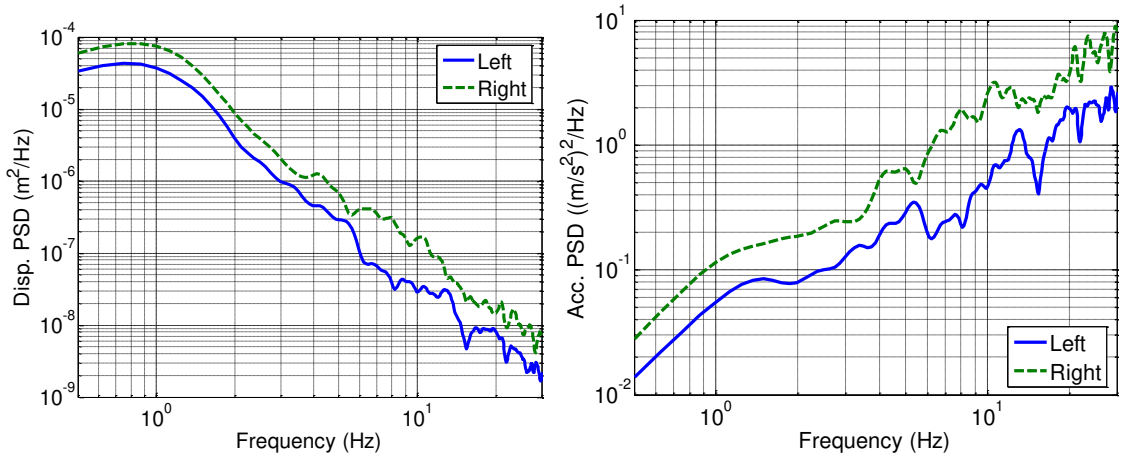

(b)

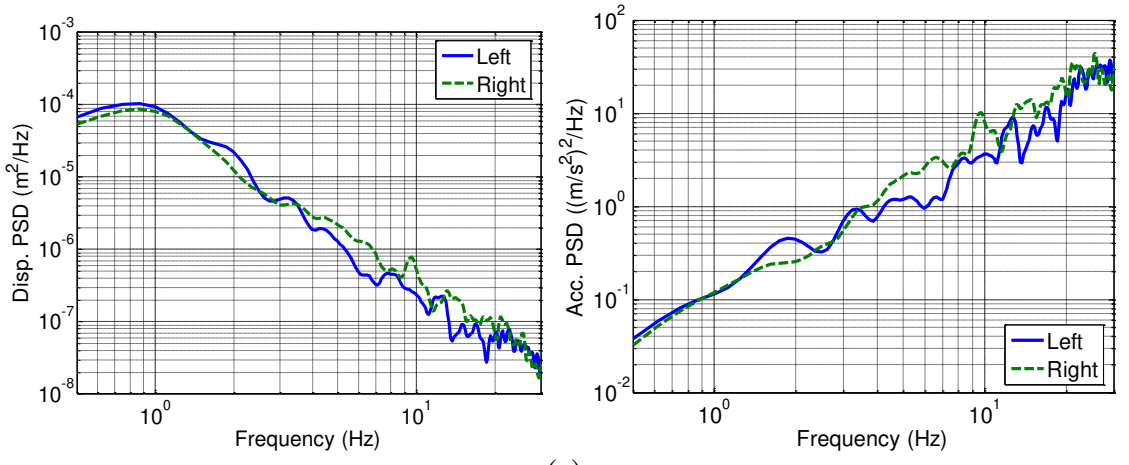

(c)

Fig. 13: Vertical displacement and acceleration temporal PSD characteristics of the selected three road profiles at a speed of 70 km/h: (a) *smooth*; (b) *medium-rough*; and (c) *rough*.

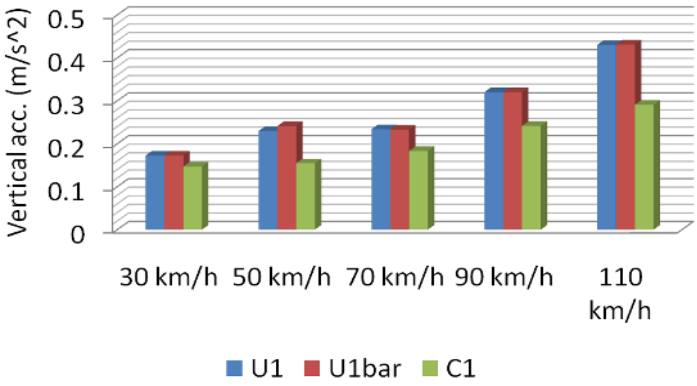

(a)

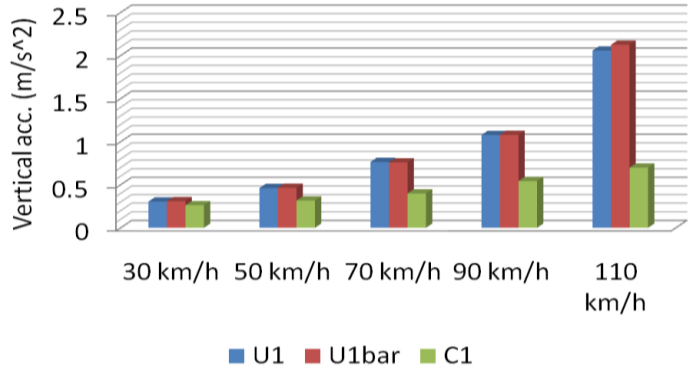

(b)

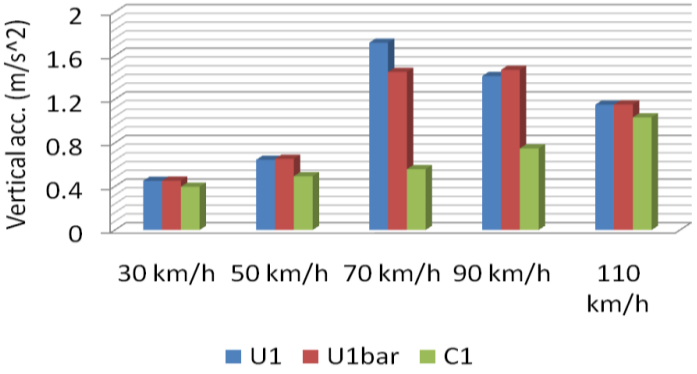

(c)

Fig. 14: Comparisons of the sprung mass vertical ride responses with different suspension configurations under different road conditions: (a) *smooth*; (b) *medium-rough*; and (c) *rough*.

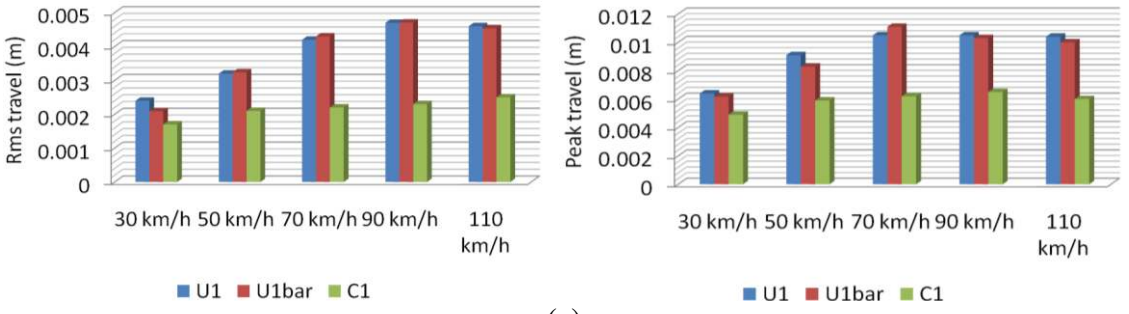

(a)

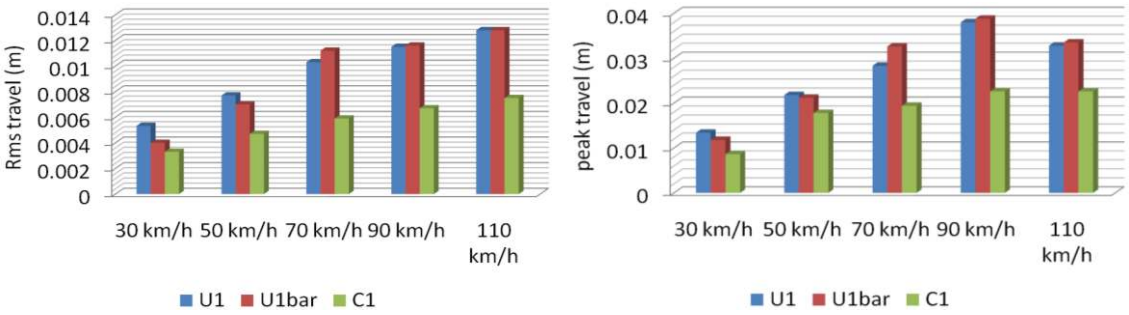

(b)

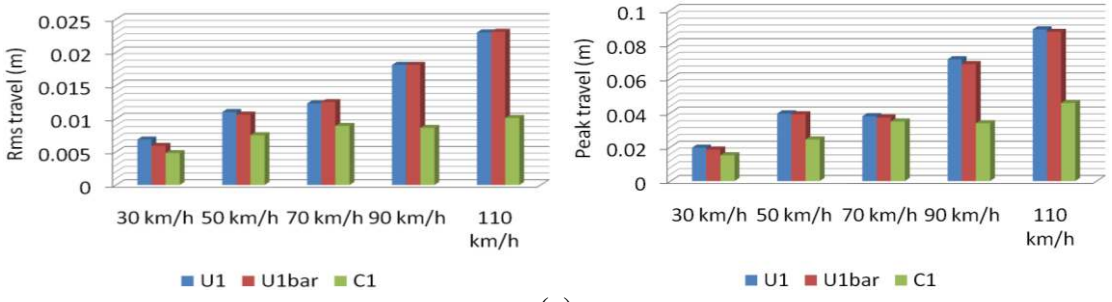

(c)

Fig. 15: Comparisons of the front-left suspension travel with different suspension configurations under different road conditions: (a) responses under *smooth* road inputs; (b) responses under *medium-rough* road inputs; (c) responses under *rough* road inputs.

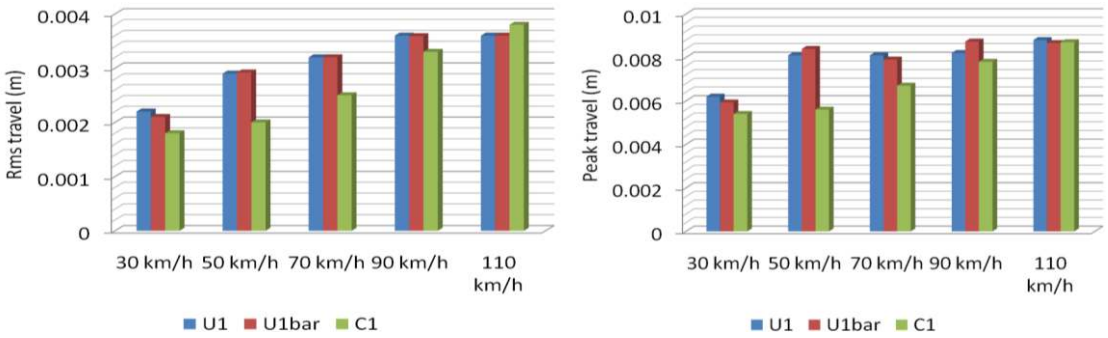

(a)

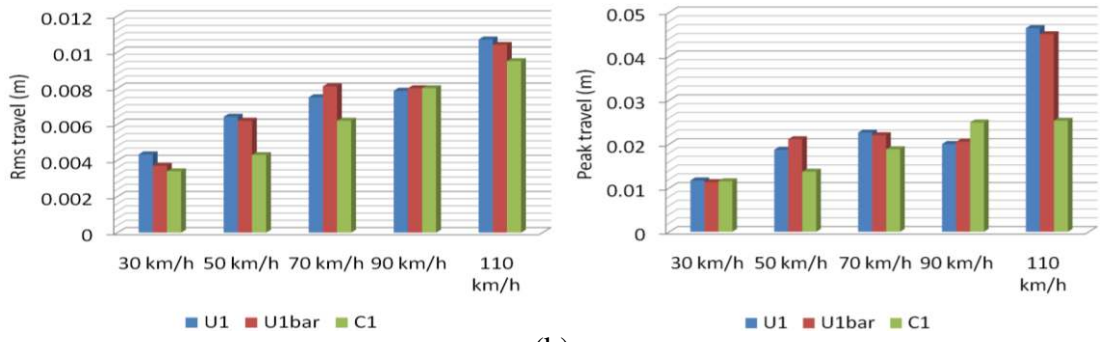

(b)

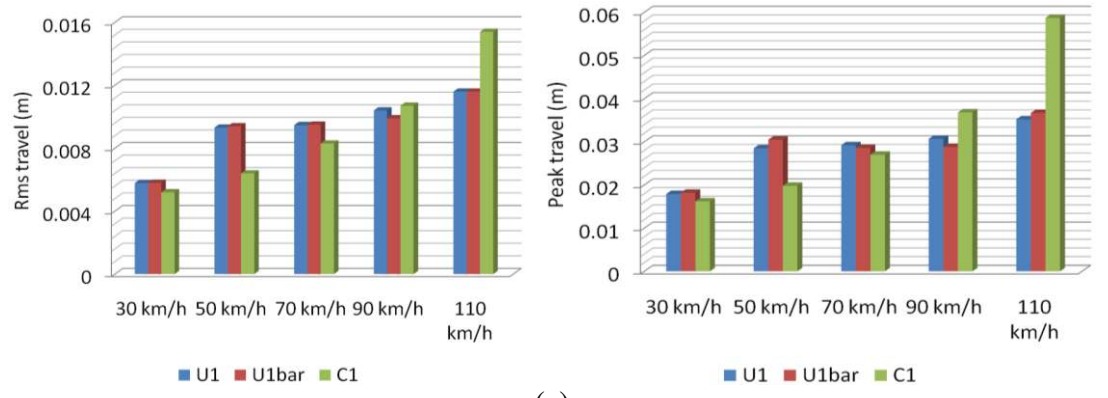

(c)

Fig. 16: Comparisons of the rear-right suspension travel with different suspension configurations under different road conditions: (a) responses under *smooth* road inputs; (b) responses under *medium-rough* road inputs; (c) responses under *rough* road inputs.

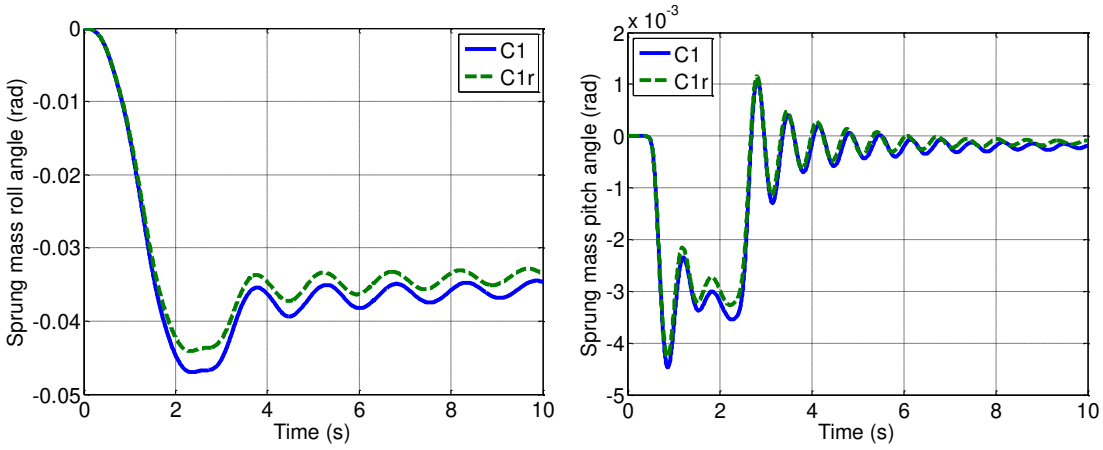

(a) (b)

Fig. 17: Dynamic responses of the vehicle with different suspension systems under a braking-in-a-turn maneuver on the dry surface: (a) sprung mass roll angle; and (b) sprung mass pitch angle.

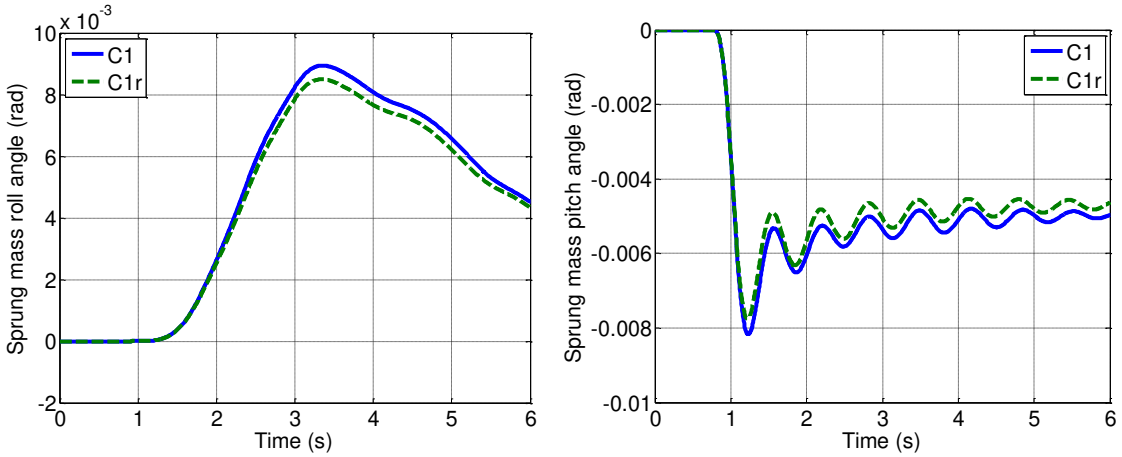

(a) (b)

Fig. 18: Dynamic responses of the vehicle with different suspension systems under split-μ straight-line braking: (a) sprung mass roll angle; and (b) sprung mass pitch angle.